# Bimodal dendritic processing in basket cells drives distinct memory-related oscillations.

Alexandra Tzilivaki[1,2,3 *], Matthew Evan Larkum[1,2,3,4], Dietmar Schmitz[1,2,3,5,6 * #]

[1]Charité-Universitätsmedizin Berlin, corporate member of Freie Universität Berlin, Humboldt-Universität Berlin, and Berlin Institute of Health, Neuroscience Research Center, 10117 Berlin, Germany

[2]Einstein Center for Neurosciences, Chariteplatz 1, 10117 Berlin, Germany

[3]NeuroCure Cluster of Excellence, Chariteplatz 1, 10117 Berlin, Germany

[4]Department of Biology, Humboldt Universität zu Berlin, Berlin 10117, Germany

[5]German Center for Neurodegenerative Diseases (DZNE), 10117 Berlin, Germany

[6]Bernstein Center for Computational Neuroscience, Humboldt-Universität zu Berlin, Philippstrasse. 13, 10115 Berlin, Germany

* Correspondence: dietmar.schmitz@charite.de , alexandra.tzilivaki@charite.de

# Main/Lead contact author

## Abstract

Hippocampal oscillations span from slow to high-frequency bands that are linked to different memory stages and behavioral states. We show that fast spiking basket cells (FSBCs) with bimodal nonlinear dendritic trees modulate these oscillations. Supralinear FSBC dendritic activation enhances high-frequency oscillations, while sublinear activation increases slow oscillatory power, adjusting the Excitation/Inhibition balance in the network. This underscores a new link between FSBCs nonlinear dendritic integration and memory-related oscillations.

## Main

Hippocampal oscillations exhibit a variety of distinct frequency bands[1]. For example, neuronal activity often associates with a slow local field potential (LFP) component, known as theta activity, which ranges from 3 to 10 Hz[1–3]. Additionally, hippocampal activity includes fast-frequency oscillations spanning from 30 to 200 Hz[1–5]. Both experimental and computational studies have linked these slow and fast components to different stages of hippocampal memory formation and distinct behavioral states[3,6,7]. Specifically, slow 3-10 Hz oscillations correlate with memory encoding, spatial navigation, and sensory processing[3]. Conversely, fast oscillations are associated with memory encoding and consolidation[3,6]. Notably, these fast and slow components often occur together in a phenomenon known as oscillation coupling[5,8–11] which has been proposed as a signature of working memory processing and various behavioral states (**Fig.1a**) [3,5].

To understand the cellular mechanisms behind these oscillatory events, significant efforts have been made to delineate the effects of various subclasses of both excitatory and inhibitory hippocampal populations. Among these, PV+ GABAergic interneurons play a crucial role in both slow and fast oscillations as well as in coupled oscillatory activity[10,12–17]. However, the vast majority of research has traditionally focused on the activation or silencing of PV+ interneurons during oscillations through optogenetic and modeling approaches.

Recent computational and experimental studies reveal that PV+ interneurons exhibit diverse nonlinear dendritic computations, significantly enhancing their computational capabilities and shaping their input-output (I/O) configurations[18–23]. Notably, a subtype of PV+ interneurons, the Fast-Spiking Basket Cells (FSBCs), possesses bimodal nonlinear dendritic integration[18,19,24]. Specifically, multicompartmental biophysical modeling has shown that FSBCs have two types of co-existing nonlinear dendrites: supralinear dendrites, which can generate local dendritic spikes, and sublinear dendrites, which integrate excitatory synaptic input passively (**Figs.1b-c,S1a-d)**. While both types of nonlinear dendrites co-exist in the same tree (**Fig.1b-c,S1)**, and share similar active properties, they differ morphologically[19]. Supralinear branches have higher volume, and lower input resistance, enabling local sodium spikes (**Fig.S1a-e)**. Conversely, sublinear branches have lower volume, and higher input resistance. Thus, coincident synaptic input induces large, fast rising EPSPs that in turn activate A-type potassium channels leading to a fast repolarization of the membrane, thus preventing the generation of local sodium spikes (**Fig.S1a-d)**. These modeling predictions[19] are supported by recent experimental findings in PV+ interneurons across different hippocampal areas[18,20,21].

However, it remains unknown whether the bimodal nonlinear nature of FSBCs dendrites affects network function by modulating different memory-related oscillations. Given the involvement of FSBCs in both slow (e.g. theta-frequencies) and fast oscillations[12,25,26], we hypothesized that the supralinear or sublinear branches of FSBCs would differentially modulate FSBCs activity and, consequently, their impact on orchestrating the LFP during mnemonic functions.

To test our hypothesis, we used a previously published biologically plausible hippocampal microcircuit model[27] that includes compartmental biophysical models of pyramidal cells (PCs) with reduced morphology[27] and FSBCs with anatomical reconstructions of bimodal nonlinear dendritic trees, as in[19,27] (**TablesS1-5**, **Fig.1a**). Upon activation with a theta-like input as per[28,29], our microcircuit exhibited a slow oscillatory component coupled with a fast one (**Fig.1a,d**). In our control experiment (bimodal activation), synapses to FSBCs were placed in randomly chosen both supralinear and sublinear branches (**Fig.1a,d, 2a**). We investigated how the network would respond when keeping the amount of synaptic contacts constant but activating either only randomly chosen supralinear branches (**Fig.1e, 2b**) or only sublinear branches (**Figs.1f, 2c**) of FSBCs trees. Our model predicts that activation of the supralinear branches of the FSBCs trees supports the fast oscillatory component (**Fig.1e,2b**). In sharp contrast, activation of only sublinear branches enhances the power of the slow LFP band (**Figs 1f, 2c**). Specifically, supralinear activation results in a higher fast frequency and fast peak-frequency power compared to both bimodal and sublinear activation conditions (**Fig.2d, e**). In contrast, sublinear activation massively decreases the fast peak-frequency power compared to both bimodal and supralinear activation (**Fig.2d**), as well as the fast peak-frequency and slow power compared to supralinear activation (**Fig.2e,f**). To assess the robustness of the differential impact of supralinear vs sublinear dendritic activation in the LFP bands, we performed a sensitivity analysis on the synaptic parameters and input features. In all cases supralinear activation enhanced the peak power and peak frequency power of the fast LFP component whereas sublinear activation resulted in higher slow power compared to supralinear activation (**Fig.S2**).

***Figure 1. Bimodal dendritic integration in FBCs modulate memory-related hippocampal oscillations.*** *Schematic Illustration of the hippocampal microcircuit model. A population of 20 PCs and 2 FSBCs is activated by a theta (4 Hz) input for 1000 msec. An*

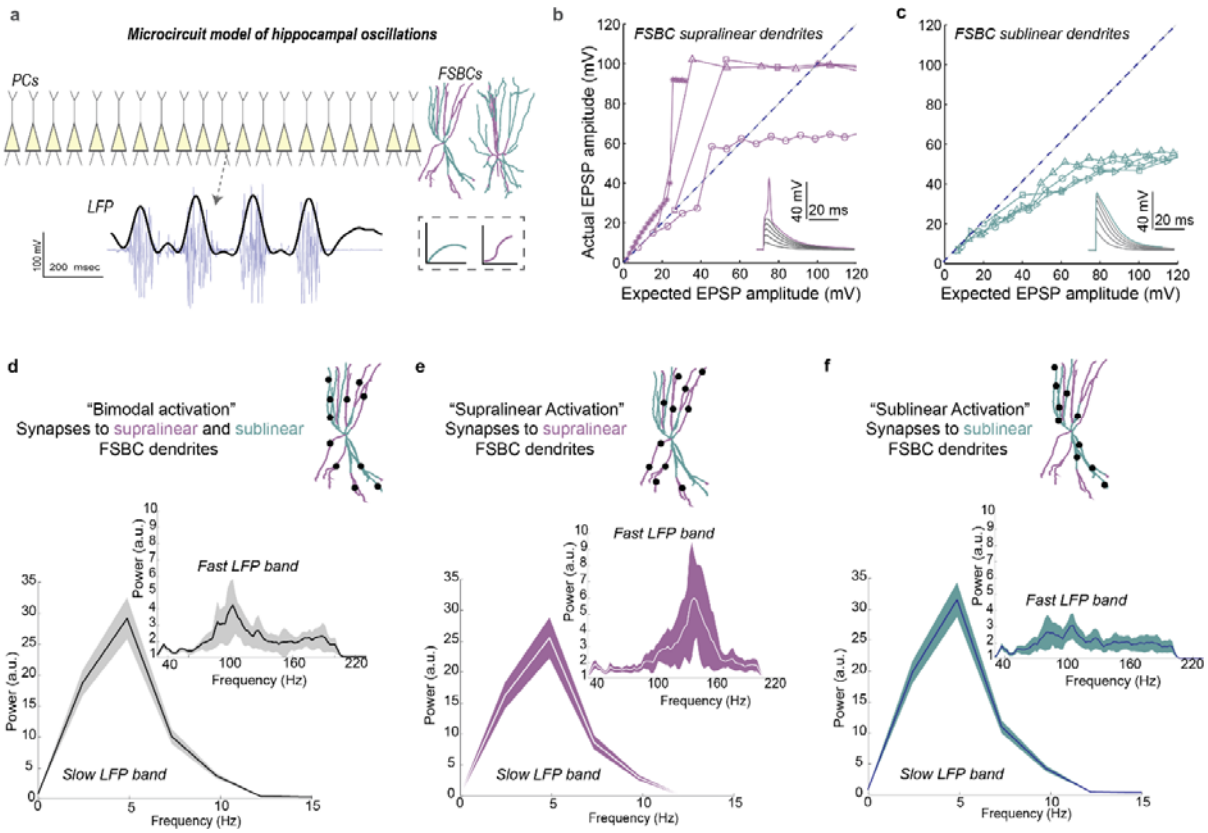


*LFP electrode is positioned nearby the PCs somata. Upon activation the model exhibits slow (bandpassed at 3-10 Hz) and fast (bandpassed at 30-200 Hz) LFP bands. The arrow indicated the in-silico electrode position. FSBCs are equipped with bimodal nonlinear trees as per Tzilivaki et al., 2019.* ***b-c.*** *Representative input-output curves from supralinear (**b**) and sublinear (**c**) dendritic branches in FSBC models, in response to synaptic stimulation. Increasing numbers of synapses (from 1 to 20 with step = 1) are uniformly distributed in every stimulated branch and are activated with a single pulse. The y-axis shows the amplitude of the dendritic EPSP caused by synaptic activation while the x-axis shows the expected EPSP amplitude that would result from the linear summation of synaptic EPSPs. The dashed line indicates linear summation. Insets show representative traces. Panels were adopted from Tzilivaki et al., 2019.* ***d-f.*** *Power Spectrum Density (PSD) plots upon bimodal (**d**), supralinear (**e**) and sublinear (**f**) activation. The number of activated synapses remain identical for all conditions. Synapses were placed in randomly chosen supralinear and sublinear branches (**d**) or in either randomly chosen supralinear (**e**) or sublinear (**f**) branches. Activation of the supralinear dendrites (**e**) supports the fast LFP signature while sublinear activation (**f**) promotes slow LFP power. Data from 30 random simulation trials.*

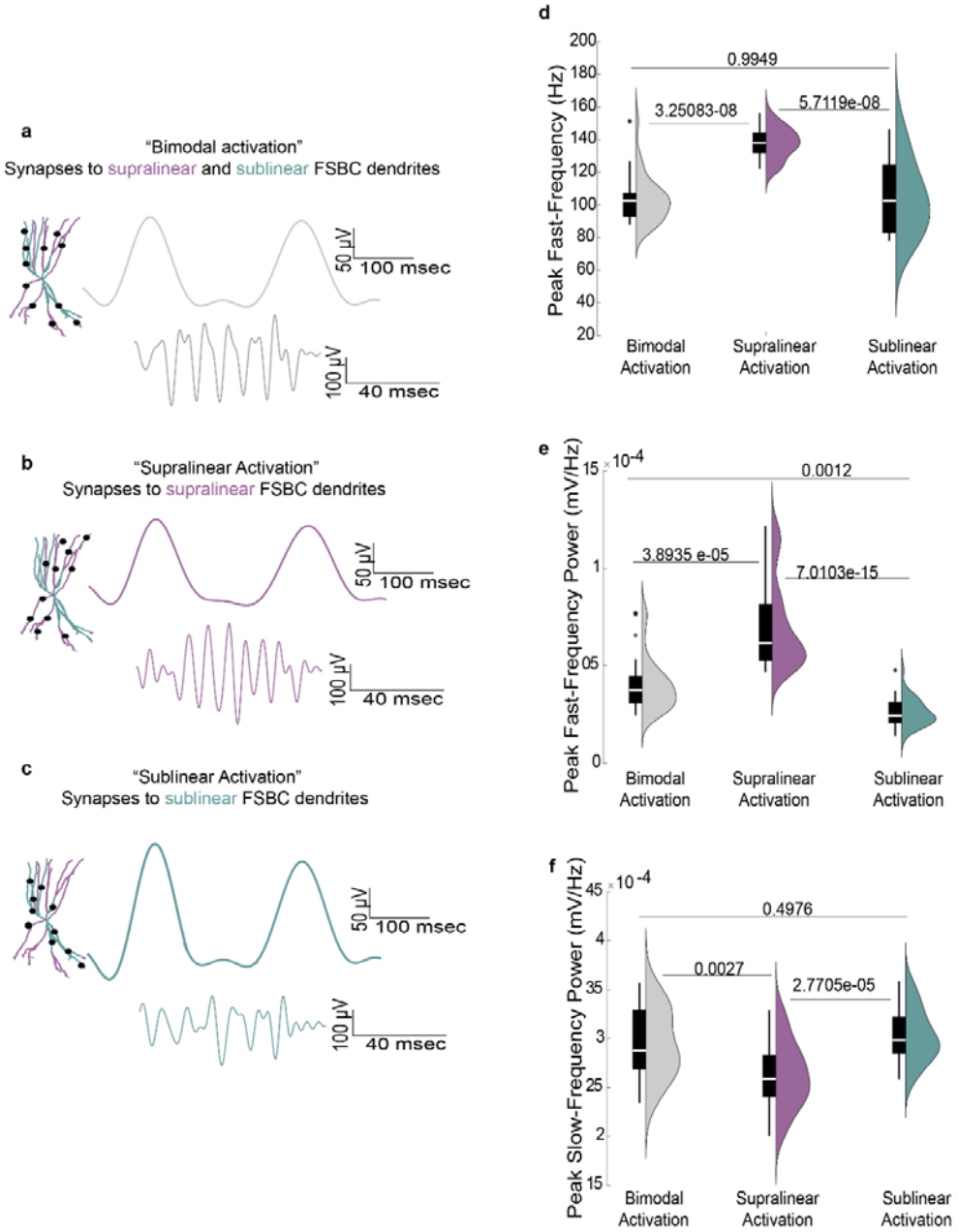


***Figure 2. LFP frequency and power are regulated by FSBC nonlinear dendritic activation.*** *(**a-c**) Schematic illustration of the activation protocols and representative traces of the evoked LFP bandpassed at slow (theta 3-10 Hz) and fast (30-200 Hz) frequences. The same number of synapses targets either both types of nonlinear dendrites (bimodal activation) (**a**) or only supralinear (**b**) or only sublinear (**c**). (**d-f**) Comparison of the peak fast-frequency (**d**) and the peak powers of the fast (**e**) and slow (**f**) LFP components. Data from 30 random simulation trials. Synaptic activation of supralinear dendrites of the FSBCs bimodal trees results in a higher peak fast-frequency and increased fast-frequency peak power, while reducing the peak power of slow oscillations compared to sublinear dendrite activation. Statistical comparisons across multiple groups were performed using the Kruskal-Wallis test followed by a post-hoc correction for multiple comparisons, suitable for data with unequal variance.*

Given that the number of synapses remains consistent across all three activation scenarios (bimodal, supralinear, and sublinear), we sought to understand the factors driving the observed LFP modulation. To achieve this, we analyzed the spiking activity of both the PC and FSBC populations under these conditions. Our analysis revealed that supralinear activation led to higher spike rates in FSBCs, resulting in decreased firing of the PC population compared to both bimodal and sublinear activation conditions. Conversely, activation of sublinear branches in FSBCs reduced their firing rates, thereby disinhibiting the

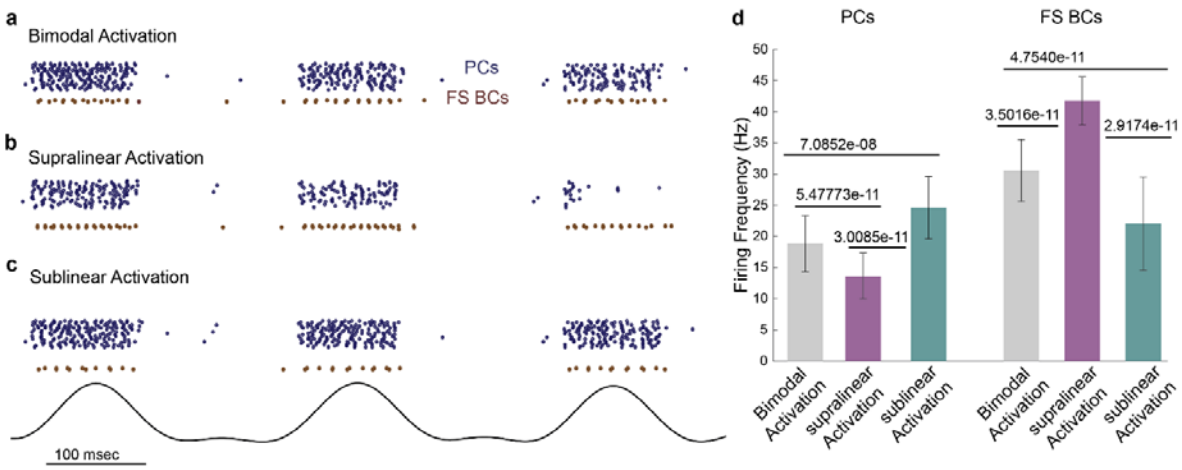


PC population (**Fig.3**).

***Figure 3. Supralinear and Sublinear FSBC dendrites differentially modulate the E/I balance in the microcircuit. (a-c)****. Representative raster plots showing the spiking activity of PCs (blue) and FSBCs (brown) across indicative theta cycles under different dendritic activation conditions: bimodal (a), supralinear (b), or sublinear (c). (**d**) Activation of a fixed number of synapses on randomly selected supralinear dendrites significantly increases the firing frequency of FSBCs, leading to a reduction in the activity of PCs when compared to bimodal (supralinear and sublinear) or purely sublinear activation. Conversely, activation of randomly selected sublinear dendrites decreases the firing frequency of FSBCs, resulting in disinhibition of the PCs. Data are based on 30 random simulation trials. Pairwise comparisons were performed using the Mann–Whitney U test.*

These observations demonstrate that FSBCs can adapt their firing patterns when activated through either supralinear or sublinear branches, despite receiving an equivalent synaptic input. Supralinear dendritic branches are characterized by larger volumes and lower input resistance[19] which facilitates enhanced forward propagation of signals. In contrast, activation of sublinear branches, which have smaller volumes and therefore higher input resistance[19], restricts forward propagation (**Fig.S1f-g**), leading to decreased firing rates of FSBCs. Consequently, this modulation alters the excitation to inhibition (E/I) balance within the network, thereby influencing the characteristic oscillatory activity observed in the LFP.

We further explored how altering the dendritic integration profile of FSBCs, specifically by manipulating them to possess purely supralinear or sublinear trees, impacts network behavior compared to the control (bimodal) trees (**Fig.S3a-b**). Leveraging the distinct morphological features of supralinear and sublinear branches in our bimodal FSBCs reconstructions, we adjusted the dendritic morphologies as per[19]. When FSBCs were

equipped with purely supralinear dendritic trees, we observed enhanced fast frequency and power compared to both bimodal and sublinear tree configurations. This configuration also maximized the firing response of FSBCs (**Fig.S3a,c-h**). Conversely, FSBCs with purely sublinear dendritic trees present reduced spike rate which increased the PCs activity (**Fig.S3h**). Sublinear FSBC trees exhibited increased slow power and decreased fast power and lower fast power compared to supralinear trees (**Fig.S3b-g**).

These simulations underscore that FSBCs take advantage of their bimodal nonlinear dendritic trees by dynamically utilizing their supralinear and sublinear dendrites to regulate the E/I balance within the network, thereby orchestrating distinct oscillatory behaviors under equivalent synaptic input conditions. Importantly, activating either only supralinear or only sublinear branches of a bimodal tree (**Figs.1-2**) exhibits similar phenotypic responses to hypothetical configurations of purely supralinear or purely sublinear trees (**Fig.S3**). This further supports the notion that the bimodal nonlinear nature of FSBCs dendrites allows for flexible modulation of network activity and oscillatory patterns crucial for hippocampal mnemonic functions.

Apart from the type of dendritic integration, the spatial arrangement of synapses also influences the firing characteristics[30]. It's well-established that supralinear dendrites tend to enhance clustered synaptic allocation, whereas sublinear dendrites prefer dispersed activation. For FSBCs, it has been observed that dispersed synaptic activation leads to higher firing frequencies compared to clustered[18,19,31]. This phenomenon is influenced by the co-existence of sublinear along with supralinear branches, coupled with their small size and the presence of A-type potassium channels[19,22,31], which discourages preference for clustered inputs. To investigate how synaptic clustering affects the oscillatory behavior of our network, we simulated the activation of the same number of synapses as in our disperse protocols (as in **Fig.S3**) but now clustered in a few randomly chosen dendrites (**Fig.S4**). As anticipated, clustered activation of sublinear FSBC trees significantly reduced their firing rates while maximizing the E/I balance in the network. Conversely, clustering synapses in supralinear trees enhanced FSBC firing rates compared to both bimodal and sublinear clustering configurations, while also decreasing the firing rates of the PCs (**Fig.S4j**). At the oscillatory level, akin to our simulations with dispersed synaptic activation, clustered synapses in supralinear FSBC trees enhanced fast LFP components, whereas synaptic clustering in sublinear trees boosted the slow LFP power (**Fig.S4a-i**). These findings underscore the dual impact of dendritic morphology and synaptic spatial arrangement on neuronal firing patterns and network oscillatory dynamics. They highlight the intricate mechanisms by which FBCs can dynamically modulate their responses and contribute to the regulation of network excitability and oscillatory activity crucial for hippocampal function.

Finally, we analyzed the Phase-Amplitude Coupling (PAC),[32] to check the slow-fast oscillation coupling in the LFP across all cases (**Fig.S5**). Indeed, the LFP response aligns with experimental findings, indicating that slow activity entrains hippocampal networks to slow-fast coupling (**Fig.S5a**)[5,9,28,33–36]. Activation of either supralinear or sublinear branches did not alter the coupling between the two oscillatory components (**Fig.S5b-f**). However, coupling was enhanced when synapses were clustered on fully sublinear dendritic trees of FSBCs. Conversely, coupling was reduced when similar clustering occurred on supralinear FSBC dendritic trees (**Fig.S5g-j**). These results indicate that as the power and frequency of the fast component decrease, it becomes more synchronized with the slower component.

Overall, while the role of interneurons in hippocampal memory-related oscillations is established[13,16,18,26], there remains a significant gap in understanding the cellular and subcellular mechanisms that enable these neurons to flexibly control memory-related rhythms. Recent studies suggest the involvement of PV+ interneuron dendrites in fast

oscillations[20,37,38], yet a direct link between interneuronal dendritic integration and their impact on slow and fast hippocampal memory-related rhythms is lacking. Our biophysical modeling provides novel insights showing that hippocampal FSBCs, a prominent subtype of PV+-positive interneurons, exhibit distinct firing patterns that modulate the excitatory-inhibitory (E/I) balance in networks independent of synaptic input quantity. Specifically, activation of supralinear dendritic branches in bimodal FSBCs (**Fig.1,2,S1**) reduces the E/I balance (**Fig.3**), thereby promoting fast oscillatory activity associated with memory consolidation (**Fig.1,2**). In contrast, activation of sublinear dendritic branches increases the E/I balance (**Fig.3**), enhancing the slow LFP signature (**Figs.1,2**), linked to memory encoding. To fully explore the impact of interneuron dendrites on memory-related oscillations, it is crucial to investigate the diversity among hippocampal interneurons[12,13,15,26]. Beyond FSBCs, other subclasses of PV+ interneurons and different inhibitory classes (e.g. SOM+ and VIP+ interneurons) are active during distinct memory-related rhythms[12,13], yet their specific dendritic integration profiles remain poorly characterized. Future studies should thus aim to dissect how dendritic nonlinear integration across different interneuron types[12,13,15,16] and PCs[39] modulate memory-related oscillations. Future experimental efforts should aim to elucidate whether distinct hippocampal and cortical inputs selectively target the supralinear or sublinear branches of bimodal FSBCs trees. Although connectivity patterns between hippocampal (e.g. CA3) and extrahippocampal (e.g. entorhinal cortices)populations to FSBCs are documented during fast oscillations[12,13,31,40], it remains unclear whether neurons from the same or different regions preferentially target these two types of nonlinear dendrites. Investigating the potential differential targeting of FSBCs' supralinear and sublinear branches during distinct memory stages, such as encoding versus consolidation, could significantly enhance our understanding of how FSBCs dynamically regulate memory-related rhythms by leveraging their diverse dendritic architectures across different oscillatory activity patterns. Our simulations suggest that bimodal nonlinear dendritic processing in FSBCs could be critical to drive different memory stages and, therefore, influence behavioral states.

**Author contributions:** AT and DS conceived the study. AT designed and run the simulations, analyzed the data, prepared the figures and wrote the manuscript. MEL and DS provided senior conceptual input on the study and methodology. DS funded and supervised the project. All authors wrote/edited the final version of the manuscript.

**Acknowledgements:** A.T. was supported by the DFG with the SFB1315-2 TP A01 Brenda Milner Award and the Einstein Center for Neurosciences Berlin Fellowship. M.E.L. was supported by the European Research Council (101055340, ERC AdG, Cortical Coupling). D.S. was supported by the Einstein Foundation Berlin, the European Research Council (ERC) under the Europeans Union's Horizon 2020 research and innovation program (BrainPlay grant, agreement no. 810580), the German Research Foundation (Deutsche Forschungsgemeinschaft [DFG], SFB-958 – project 184695641, project 431572356, FOR 3004 – project 415914819, SFB 1315 – project 327654276 and under Germany's Excellence Strategy – Exc-2049-390688087 NeuroCure), and the Federal Ministry of Education and Research (BMBF, SmartAge – project 01GQ1420B). We thank Michalis Pagkalos, Jeremie Sibille, Nikolaus Maier, and John Tukker for helpful discussions, comments and proofreading, Nelson Rebola, Yann Zerlaut, Yiota Poirazi, for comments on an earlier version of the manuscript and Daniel Parthier for feedback on the statistical analyses.

**Code and Data availability**

Scripts and datasets required to reproduce the results and figures, as well as all statistical analyses, are publicly accessible in www.github.com/AlexandraTzilivaki/Tzilivakietal2024

**Competing interests**

The authors declare no competing interests.

# Methods

**Model implementation and availability**

Simulations were conducted using NEURON (v7.6)[41] on a High-Performance Computing Cluster, utilizing 111 CPU cores on a 64-bit CentOS Linux operating system. All codes/scripts and datasets required to reproduce the results and figures, as well as all statistical analyses, are publicly accessible in www.github.com/AlexandraTzilivaki/Tzilivakietal2024

**Neuronal populations**

1. Fast Spiking Basket Cells (FSBCs)

Two multi-compartmental biophysical models of CA3 FSBCs were employed, adopted from Tzilivaki et al. (2019)[19]. These FSBCs models include detailed anatomical reconstructions of somata and dendritic trees taken from Neuromorpho database (originally published in Tukker et al. 2007[42]), (**Figure S1**). Both FSBCs feature bimodal nonlinear dendritic branches, characterized by both supralinear and sublinear branches. They are equipped with fast voltage-dependent sodium channels (gnafin), delayed rectifier potassium channels (gkdrin), slow inactivation potassium channels (gslowin), slow calcium-dependent potassium channels (gkcain), A-type potassium channels in proximal and distal dendritic regions (gkadin, gkapin), h-currents (ghin), and L-, N-, and T-type voltage-activated calcium channels (gcal, gcan, and gcat, respectively). These models have been extensively validated against experimental data and accurately capture the intrinsic features and electrophysiological responses of hippocampal FSBCs (See original reference[19] and Supplementary Information). The mean dendritic diameter and total dendritic length were measured for the supralinear and sublinear dendrites of the two FSBCs morphological reconstructions. Dendritic volume was calculated as per Tzilivaki et al. (2019)[19] using the following formula:

$$V = \pi * \left(\frac{diameter}{2}\right)^2 * length\ (\mu m^3)$$

To causally manipulate the dendritic morphologies of FSBCs to generate fully supralinear or sublinear trees (Figure S2), we performed causal manipulations according to the approach described in Tzilivaki et al. (2019)[19]. We fixed the diameter and length of all dendrites to create trees with average supralinear or sublinear dendritic volume (**Figure S1B**), which dictated the integration mode as shown in the original modeling publication. Dendritic Input Resistance was calculated using the following formula:

$$Rin = \frac{DV}{I}\left(\frac{mV}{nA}\right)$$

where I = −100 pA injected in each dendritic branch and DV is the generated IPSP.

For more detailed information about the FSBC models, please refer to the relevant publication[19] and **Tables S1-2, 4-5**.

2. Pyramidal Cells (PCs)

Biophysically relevant hippocampal PC models (n = 20) were adopted from Hadler et al. (2024)[27]. These models consist of somata and proximal, distal, and basal dendritic branches. PCs include a Ca2+ pump and buffering mechanism, Ca2+ activated slow AHP and medium AHP potassium (K+) currents, an HVA L-type calcium (Ca2+) current, an HVA R-type Ca2+current, an LVA T-type Ca2+ current, an h-current, a fast sodium (Na+) current, a delayed rectifier K+ current, a slowly inactivating K+ M-type current, and a fast inactivating K+ A-type current. These current mechanisms were non-uniformly distributed along the somatodendritic compartments. They were validated based on *in vitro* data to replicate the electrophysiological profile and basic dendritic architecture of hippocampal CA3 PCs[27,43]. The PC models do not include detailed nonlinear dendritic trees, as this was beyond the scope of this study. Incorporating realistic anatomical reconstructions for PCs would have significantly increased computational complexity and reduced simulation speed. For more information, see Hadler et al. (2024)[27] and **Tables S3-5**.

**Synaptic properties**

The PC models were equipped with AMPA, NMDA, and γ-aminobutyric acid type A (GABAA) synapses, while the FSBCs included Ca2+ permeable AMPA (CP-AMPA), NMDA, GABAA, and autaptic GABAA synapses. The synaptic conductance values for every connection type were calibrated based on experimental[44–47] and modelling studies[19] and are listed in **Table S5**
To ensure the robustness of our finding we repeated the simulations upon increased or decreased synaptic conductance values (15% change) (see sensitivity analysis Figure S2)

**Hippocampal Microcircuit**

The hippocampal microcircuit configuration was adopted from Hadler et al. (2024)[27]. The model consists of 20 PCs and 2 FSBCs. In each random simulation trial (n = 30), each PC contacted up to seven (7) randomly chosen PCs with one AMPA and one NMDA synapse activation per contact. Each FSBC received synaptic input from fifteen (15) randomly chosen PCs in each simulation trial. Additionally, each PC received thirteen (13) feedback inhibitory GABAergic inputs from each FSBC per simulation trial. Each FSBC formed five (5) GABAergic synapses per simulation trial and was self-inhibited through autapses. For further details, see the Simulation Paradigms chapter and Hadler et al. (2024)[27].

**Simulation Paradigms**

Input

The microcircuit is activated by a theta entrained presynaptic population as per Turi et al., 2018[48]. The input was modeled as an artificial presynaptic population (N=22) using NEURON's VecStim function. The spike times of the presynaptic population were generated using a sinusoidal theta like filter that was applied so to account for theta like modulated spike times.

Thata like probability formula (as per [48]):

$$p(t) = (\sin\left(2.0 * pi * \frac{f_{theta*spike}}{1000.0} + phi_{theta}\right) + 1.0)/2.0$$

Where:

- spike = the spike time in msec (float)
- f_theta = theta-cycle frequency in Hz. (float)

For the simulations shown in Figures 1-3 and Supplementary Figures 3-5, f_theta=4 Hz. For the sensitivity analysis simulations as shown in Supplementary Figure 2, we changed the input the theta frequency to f_theta=5Hz.

- phi_theta= theta cycle phase in radians.

For the simulations shown in Figures 1-3 and Supplementary Figures 3-5, phi_theta=0 (equal to 0 radians). For the sensitivity analysis simulations as shown in Supplementary Figure 2, we shifted the input phase so phi_theta=0.5 (equal to 180 radians).

If the probability p(t) is greater than 0.7 a spike is generated for the specific artificial neuron (n=22). Every input neuron has its own theta modulated spike train.

Each PC received input from 5 artificial presynaptic neurons, while each FSBC received input from 7 artificial presynaptic neurons. Although the input was sufficient to activate the PC population due to its reduced morphology, 7 artificial presynaptic neurons were insufficient to evoke spiking activity in the FSBC models, given their realistic complex anatomical reconstructions. This subthreshold activation was selected to ensure that FSBCs were primarily engaged in the network due to the local inputs they received from PCs.

1. **Simulations**

The microcircuit model was simulated for approximately 12,000 milliseconds (ms) with a time step of 0.1 ms. The first 200 ms were excluded from the analysis to allow the model to reach an equilibrium state. For the dispersed protocols, synapses to FSBCs (both input and local PC-to-FSBC synapses) were randomly assigned to dendrites, meaning one randomly chosen dendrite received one pair of NMDA and CP-AMPA synapses. For the clustered protocol (Supplementary Figure S4), the same total amount of synapses was placed in 4 randomly chosen dendrites (cluster size: 5-7 synapses (per dendrite) Data represent the results (mean and standard deviation values (std)) of thirty (30) random simulation trials for each protocol. In every trial, the total number of synaptic contacts and the connectivity ratios remained identical, but different randomly chosen neurons (from both PC and FSBC populations) were connected to different random neurons. Additionally, in each trial, different dendrites from both PCs and FSBCs were randomly chosen and synapses were activated at different parts of the chosen dendrites. This approach ensured that the results reflected the diversity, especially of the FSBCs trees, in bimodal activation protocols. Furthermore, two different anatomical reconstructions were used for our FSBC models to account for FSBCs morphological variability (see relevant chapter).

## 2. LFP simulation and Spectral analysis

To record the Local Field Potential (LFP), an *in silico* electrode was simulated based on NEURON's extracellular function, following the modelling approach of Vladimirov et al. (2013)[49]. The electrode was placed close to the PCs somata and remained in the exact same position throughout the execution of all protocols and simulation trials. The

sampling frequency was set at 10 kHz. Despite the microcircuit model's small size, it efficiently generated fast and slow oscillations comparable to experimental observations[5,11,32,35] while maintaining low computational complexity and demands.

The *in silico* LFP datasets were band-passed at two respective bands: slow (3 – 10 Hz) and fast (30-200 Hz). Slow and fast Peak-Frequency powers and peak Fast frequency were determined using custom-made MATLAB scripts (MATLAB, The MathWorks Inc., Natick, MA; Torrence and Compo 1998) utilizing the p-welch function (0.4 Hz resolution) and visualized as Power-Frequency plots. Phase-Amplitude Coupling (PAC) analysis was conducted using Comodulogram generation and the calculation of the modulation index (MI) metric that were adopted from Tort et al. (2008)[50]. Wavelet phase was calculated at 15 levels from 1-15 Hz, and the amplitude at 50 levels from 30-180 Hz. The MI was obtained by measuring the divergence of the observed amplitude distribution from the uniform distribution.

**Statistical Analysis**

Statistical analyses for multigroup comparisons were performed using the Kruskal-Wallis test, followed by a post-hoc correction for multiple comparisons (multcompare function Matlab). For pairwise comparisons where data exhibited unequal variance, p-values were calculated using the Mann-Whitney U test.

## Supplementary Information

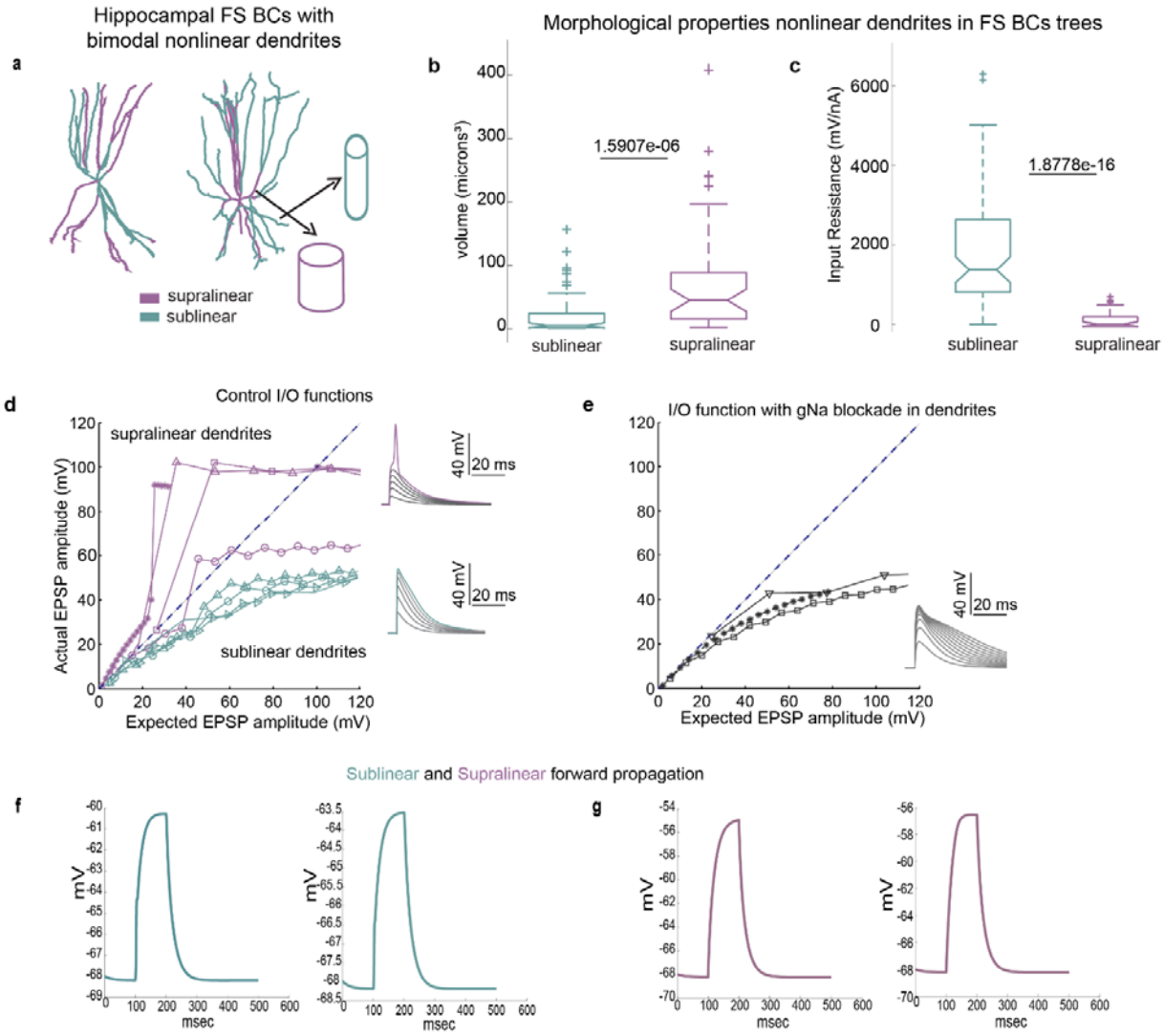


**Figure S1**. **Mechanisms of bimodal nonlinear dendritic integration in Multicompartmental Models of Hippocampal FSBCs.**

**a**. Illustration of the morphological characteristics of supralinear and sublinear dendrites in bimodal FSBC models. Supralinear dendrites (purple) are larger, whereas sublinear dendrites (blue) are longer and thinner. **b-c**. Discriminative features between dendrite types: supralinear dendrites have larger volumes (b) and lower input resistance (c) compared to sublinear dendrites. Statistical significance was determined using the Mann–Whitney U test. **d-e**. Supralinear dendrites (purple) are capable of generating local sodium-dependent spikes, whereas sublinear dendrites (blue) cannot (d). Blocking active sodium conductances in FSBC dendrites completely abolishes the supralinear mode (e). **f-g**. Forward propagation efficiency in bimodal nonlinear dendrites of FSBCs: Current injection (100 pA) at randomly selected dendrites and recording at the soma show that sublinear branches (f) propagate signals less effectively compared to supralinear branches (g). Panels a,d,e were adopted from [19]

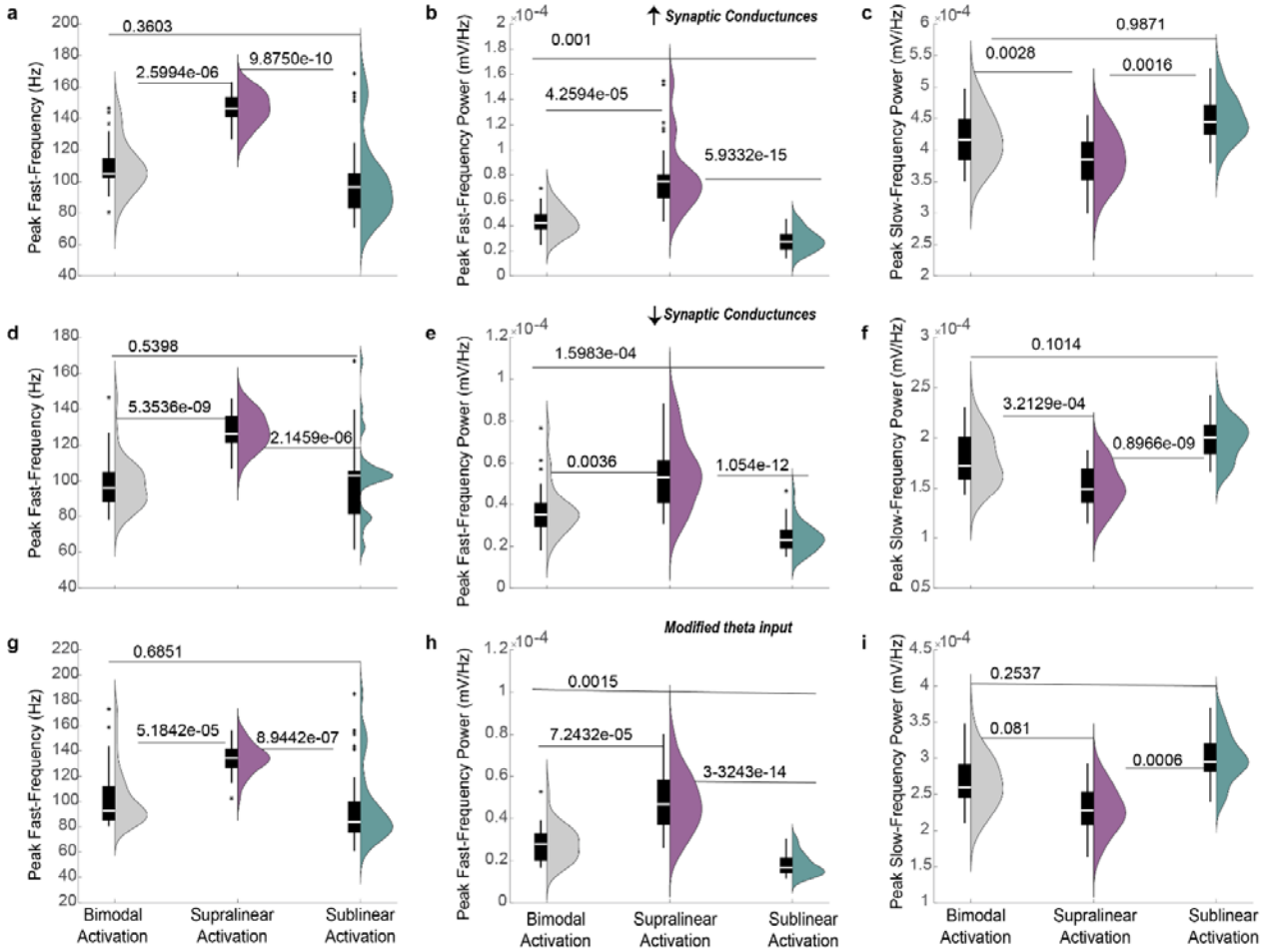


**Figure S2. Sensitivity Analysis on Synaptic and Input Parameters (Related to Figure 2). a-c**. 15% increase in the synaptic conductance values (applied to both input and network synapses for/from both PCs and FSBCs) do not alter the enhancement of fast peak frequency and power observed with supralinear activation. **d-f**. 15% reduction of the synaptic conductance values (for both input and network synapses involving PCs and FSBCs) also maintain the observed increase in fast peak frequency and power upon supralinear activation. **g-i**. Modifications to input parameters (input phase shifted 180°, peak frequency 5 Hz) similarly do not affect the enhancement of fast peak frequency and power driven by supralinear activation. Statistical analyses for multigroup comparisons were performed using the Kruskal-Wallis test, followed by a post-hoc correction for multiple comparisons.

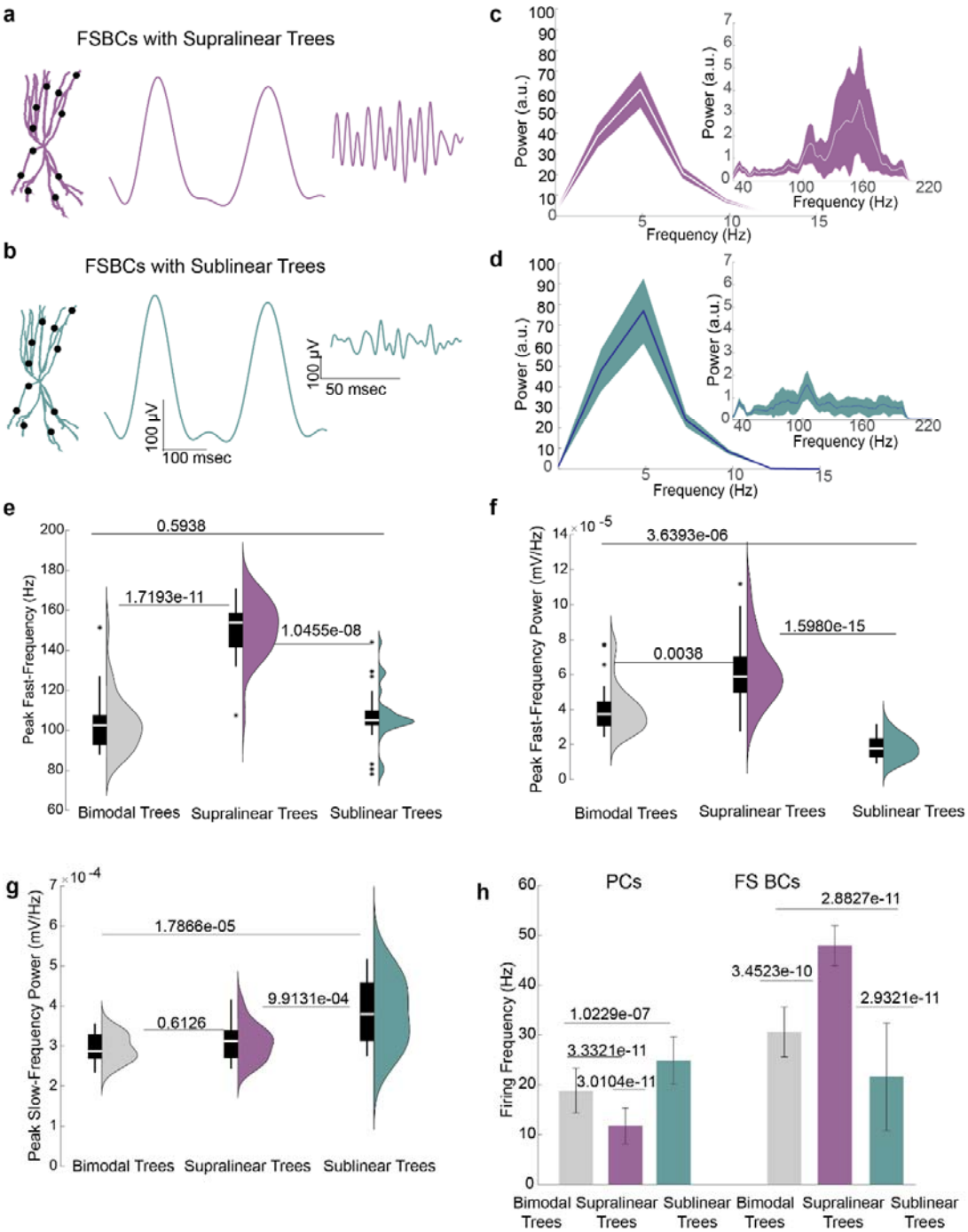


**Figure S3. Differential Modulation of Slow and Fast LFP Components by Supralinear and Sublinear FSBC Dendritic Trees.**

**a**. Activation of FSBCs equipped with purely supralinear dendritic trees, showcasing representative LFP traces bandpassed at slow (3-10 Hz) and high (30-200 Hz) frequencies. **b**. Similar to **a** but displaying activation of FSBCs with purely sublinear dendritic trees. **c-d**. Power Spectrum Density (PSD) plots of the LFP evoked when FSBCs are equipped with

purely supralinear (c) or purely sublinear (d) dendritic trees, highlighting differences in frequency response. **e-g**. Comparative analysis of the peak fast-frequency (e) and peak power of fast (f) and slow (g) oscillations for FSBCs with bimodal (grey), supralinear (purple), or sublinear (blue) dendritic trees. Data are derived from 30 random simulation trials. **h**. Firing activity of the PCs and FSBCs populations within the microcircuit network across 30 random simulation trials. Activation of supralinear FSBC dendritic trees results in a decreased E/I balance compared to both bimodal (control) and sublinear trees. Statistical analyses for multigroup comparisons were conducted using the Kruskal-Wallis test followed by a post-hoc correction for multiple comparisons. Paired comparisons and p-values were calculated using the Mann-Whitney U test for data with unequal variance.

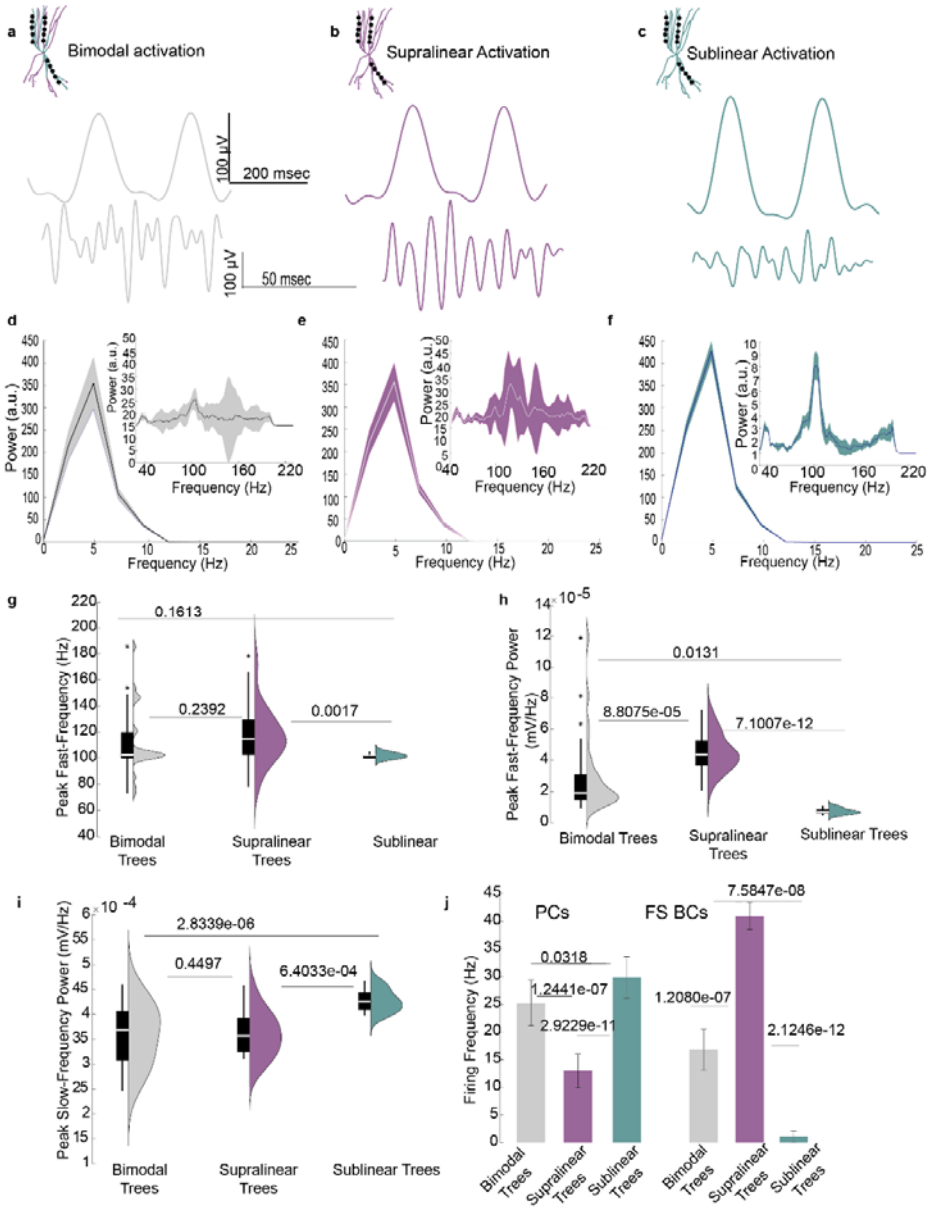

**Figure S4. Impact of Clustered Synaptic Activation on LFP and E/I Balance in Bimodal, Supralinear, and Sublinear FSBC Dendritic Configurations. a**. Activation of FSBCs with bimodal nonlinear dendrites (control configuration), showing representative LFP traces for slow (3-10 Hz) and fast (30-200 Hz) frequencies. Synapses are clustered in a few randomly chosen supralinear or sublinear branches. **b**. Activation of FSBCs with purely supralinear dendritic trees, showing LFP traces under clustered synaptic activation. **c**. Activation of FSBCs with purely sublinear dendritic trees, similar to conditions in a and b, illustrating the effect of clustered synaptic activation on LFP traces. **d-f**. Power Spectrum Density (PSD) plots for LFPs under clustered synaptic conditions in FSBCs with bimodal (d), supralinear (e), and sublinear (f) dendritic configurations. **g-i**. Comparison of peak frequency (g) and peak power for the fast LFP component (30-200 Hz) (h), and peak power for the slow LFP component (i), across dendritic configurations. **j**. Firing activity of PC and FSBC populations in the microcircuit network from 30 random simulation trials. Clustering in supralinear FSBC dendritic trees decreases the E/I balance in the network compared to bimodal (control) or sublinear trees. Statistical analyses for multigroup comparisons were conducted using the Kruskal-Wallis test followed by a post-hoc correction for multiple comparisons. Paired comparisons and p-values were calculated using the Mann-Whitney U test for data with

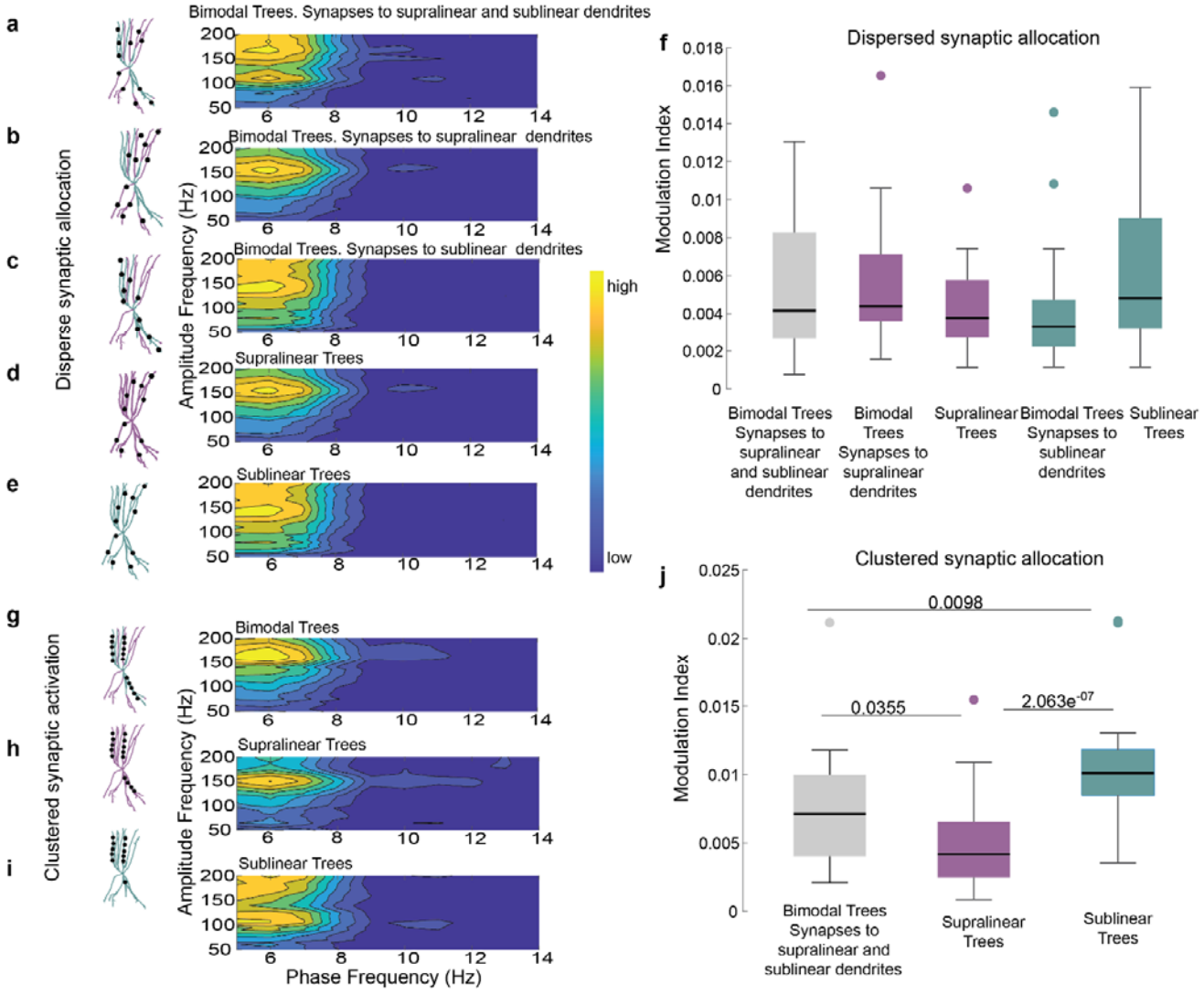


unequal variance.

**Figure S5. Slow-Fast Oscillation Coupling in the Microcircuit Model Under Various Dendritic and Synaptic Configurations in FSBCs. a-e**. Representative comodulograms illustrating the slow-fast coupling for the protocols detailed in Figures 2 and S3. These visualizations provide insights into the phase-amplitude coupling dynamics under different synaptic and dendritic configurations. Data from 30 random simulation trials are represented. **f**. Coupling analysis shows that synaptic distribution in a dispersed configuration across bimodal, purely supralinear, or purely sublinear FSBC dendritic trees does not affect slow-fast oscillation coupling. **g-i**. Similar to a-e but showcasing comodulograms for a clustered synaptic arrangement (detailed in Figure S4), using the same number of synapses as in the dispersed experiments. **j.** MI indicates that slow-fast oscillation coupling decreases when synapses are clustered in purely sublinear dendritic trees compared to other configurations. Multigroup comparisons were performed using the Kruskal-Wallis test followed by a post-hoc correction for multiple comparisons for multi-group data with unequal variance. This statistical approach was chosen to accommodate the diversity in the data from 30 random simulation trials.

***Table S1. Active properties of Fast Spiking Basket Cell (FSBC) Models***

| *Ion channel ($S/cm^2$)* | *Soma* | *Axon* | *Proximal dendrites* | *Distal Dendrites* |
|---|---|---|---|---|
| *$Na_v$* | 0.396 | 1.296 | 0.018 | 0.014 |
| *$H_v$* | 0.00001 | X | x | X |

**values as per [19,51,52]*

***Table S2. Passive properties of FSBCs***

| | *Soma* | *Axon* | *Proximal dendrites* | *Distal Dendrites* |
|---|---|---|---|---|
| *Leak conductance (g_pas)*[53] | 1.315e-4 $S/cm^2$ | 3.55e-6 $S/cm^2$ | 1.315e-4 $S/cm^2$ | 1.34e-5 $S/cm^2$ |
| *Resting Membrane Potential (e_pas)*[53,54] | -68 mV | -68 mV | -68 mV | -68 mV |
| *Membrane capacitance (cm)*[53] | 1.2 $uf/cm^{-2}$ | 1.2 $uf/cm^{-2}$ | 1.2 $uf/cm^{-2}$ | 1.2 $uf/cm^{-2}$ |
| *Axial Resistance (Ra)*[53] | 172 ohm/ cm | 172 ohm/ cm | 142 ohm/ cm | 142 ohm/ cm |
| *$Can_v$* | x | X | 0.00003 | 0.00003 |
| *$Cat_v$* | x | X | 0.0002 | 0.0002 |
| *Calcium buffering dynamics* | Yes | No | Yes | Yes |

**values as per [19,53,54]*

***Table S3. Passive Parameters and Active Conductance Values of the Pyramidal Cell (PC) Model***

| ***Mechanism*** | **Soma** | **Proximal Apical** | **Distal Apical** | **Basal** |
|---|---|---|---|---|

| | | Dendrite(n=1) | Dendrites (n=2) | Dendrites (n=2) |
|---|---|---|---|---|
| *Leak conductance [S/cm2 ]* | 0,0002 | 0,0002 | 0,0002 | 0,0002 |
| *Na+ conductance [S/cm2]* | 0,0105 | 0,0084 | 0,0084 | 0,0084 |
| *Delayed rectifier K+ conductance [S/cm2]* | 0,00086 | 0,00086 | 0,00086 | 0,00086 |
| *Proximal A-type K+ conductance [S/cm2 ]* | 0,0075 | 0,015 | - | 0,0075 |
| *Distal A-type K+ conductance [S/cm2 ]* | - | - | 0,04875 | - |
| *M-type K+ conductance [S/cm2 ]* | 0.06 | 0.06 | - | 0.06 |
| *Ih conductance [S/cm2]* | 0.00005 | 0.0001 | - | 0.00005 |
| *L-type Ca2+ conductance [S/cm2 ]* | 0.0007 | 0.00003 | - | 0.00003 |
| *R-type Ca2+ conductance [S/cm2 ]* | 0.0003 | 0.00003 | - | - |
| *T-type Ca2+ conductance [S/cm2 ]* | 0.00005 | 0.0001 | - | 0.0001 |
| *Ca2+ -dependent sAHP K+ conductance [S/cm2]* | 0.0015 | 0.001 | - | 0.0005 |
| *Ca2+-dependent mAHP K+ conductance [S/cm2 ]* | 0,9 | 0,03 | - | 0,08 |
| *Membrane capacitance Cm [µF/cm2]* | 1 | 1 | 1 | 1 |
| *Membrane resistance Rm [Ohm cm2]* | 6000 | 6000 | 6000 | 6000 |
| *Axial resistance Ra [Ohm cm]* | 150 | 150 | 150 | 150 |

**values as per [27]*

***Table S4. Electrophysiological properties of the PCs and FSBCs models***

| | Value |
|---|---|
| *Rheobase (pA)* | 200 (PC) / 150 +/- 10 (FSBC) |
| *Input Resistance (MΩ)* | 142 (PC) / 97+/- 30 (FSBC) |
| *Spike Threshold (mV)* | -43,11 (PC) / -37 +/-1 (FSBC) |
| *Spike Overshoot (mV)* | 30 (PC) / 48 +/- 1 (FSBC) |
| *Resting Membrane Potential (mV)* | -70 (PC) / -68 (FSBC) |

***Table S5. Synaptic conductance weight values of the PC and FSBC models.***

| *Synapse Type* | Pyramidal model | FSBC model |
|---|---|---|
| *INPUT AMPA* | 0,00272 | - |
| *INPUT NMDA* | 0,0053 | 0.00032 |
| *INPUT CA++ PERMEABLE (CP)-AMPA* | - | 0.00075 |
| *AMPA* | 0,0017 | - |
| *CP-AMPA* | - | 0,0034 |

| | | |
|---|---|---|
| *NMDA* | 0,0051 | 0.00144 |
| *GABA* | 0,0068 | 0,0051 |
| *Autapse GABA* | - | 0,007 |

**values based on*[19,27,44,45,47,55]

**References:**


1. Buzsáki, G. & Draguhn, A. Neuronal Oscillations in Cortical Networks. *Science (80-. ).* **304**, 1926–1929 (2004).
2. Jackson, J. & Skinner, F. K. Hippocampus, Theta, Gamma, and Cross-Frequency Coupling. in *Encyclopedia of Computational Neuroscience* 1–11 (Springer New York, 2018). doi:10.1007/978-1-4614-7320-6_30-2.
3. Lisman, J. E. & Jensen, O. The Theta-Gamma Neural Code. *Neuron* **77**, 1002–1016 (2013).
4. Griffiths, B. J. & Jensen, O. Gamma oscillations and episodic memory. *Trends Neurosci.* **46**, 832–846 (2023).
5. Tort, A. B. L., Scheffer-Teixeira, R., Souza, B. C., Draguhn, A. & Brankačk, J. Theta-associated high-frequency oscillations (110–160Hz) in the hippocampus and neocortex. *Prog. Neurobiol.* **100**, 1–14 (2013).
6. Buzsáki, G. & Wang, X.-J. Mechanisms of Gamma Oscillations. *Annu. Rev. Neurosci.* **35**, 203–225 (2012).
7. Buzsáki, G. Two-stage model of memory trace formation: A role for “noisy” brain states. *Neuroscience* **31**, 551–570 (1989).
8. Jackson, J., Goutagny, R. & Williams, S. Fast and Slow Gamma Rhythms Are Intrinsically and Independently Generated in the Subiculum. *J. Neurosci.* **31**, 12104–12117 (2011).
9. Zhang, X. *et al.* Impaired theta-gamma coupling in APP-deficient mice. *Sci. Rep.* **6**, 21948 (2016).
10. Wulff, P. *et al.* Hippocampal theta rhythm and its coupling with gamma oscillations require fast inhibition onto parvalbumin-positive interneurons. *Proc. Natl. Acad. Sci.* **106**, 3561–3566 (2009).
11. Schomburg, E. W. *et al.* Theta Phase Segregation of Input-Specific Gamma Patterns in Entorhinal-Hippocampal Networks. *Neuron* **84**, 470–485 (2014).
12. Tzilivaki, A. *et al.* Hippocampal GABAergic interneurons and memory. *Neuron* **111**, 3154–3175 (2023).
13. Topolnik, L. & Tamboli, S. The role of inhibitory circuits in hippocampal memory processing. *Nat. Rev. Neurosci.* **23**, 476–492 (2022).
14. Cardin, J. A. *et al.* Driving fast-spiking cells induces gamma rhythm and controls sensory responses. *Nature* **459**, 663–667 (2009).
15. Pelkey, K. A. *et al.* Hippocampal gabaergic inhibitory interneurons. *Physiol. Rev.* **97**, 1619–1747 (2017).
16. Allen, K. & Monyer, H. Interneuron control of hippocampal oscillations. *Curr. Opin. Neurobiol.* **31**, 81–87 (2015).

17. Lucas, E. K. & Clem, R. L. GABAergic interneurons: The orchestra or the conductor in fear learning and memory? *Brain Res. Bull.* **141**, 13–19 (2018).

18. Tzilivaki, A., Kastellakis, G., Schmitz, D. & Poirazi, P. GABAergic Interneurons with Nonlinear Dendrites: From Neuronal Computations to Memory Engrams. *Neuroscience* **489**, 34–43 (2022).

19. Tzilivaki, A., Kastellakis, G. & Poirazi, P. Challenging the point neuron dogma: FS basket cells as 2-stage nonlinear integrators. *Nat. Commun.* **10**, 3664 (2019).

20. Chiovini, B. *et al.* Dendritic Spikes Induce Ripples in Parvalbumin Interneurons during Hippocampal Sharp Waves. *Neuron* **82**, 908–924 (2014).

21. Cornford, J. H. *et al.* Dendritic NMDA receptors in parvalbumin neurons enable strong and stable neuronal assemblies. *Elife* **8**, (2019).

22. Hu, H. & Vervaeke, K. Synaptic Integration in Cortical Inhibitory Neuron Dendrites. *Neuroscience* **368**, 115–131 (2018).

23. Katona, G. *et al.* Roller Coaster Scanning reveals spontaneous triggering of dendritic spikes in CA1 interneurons. *Proc. Natl. Acad. Sci. U. S. A.* **108**, 2148–2153 (2011).

24. Cornford, J. H. *et al.* Dendritic NMDA receptors in parvalbumin neurons enable strong and stable neuronal assemblies. *Elife* **8**, (2019).

25. Chamberland, S. & Topolnik, L. Inhibitory control of hippocampal inhibitory neurons. *Front. Neurosci.* **6**, 1–13 (2012).

26. Klausberger, T. & Somogyi, P. Neuronal Diversity and Temporal Dynamics: The Unity of Hippocampal Circuit Operations. *Science (80-. ).* **321**, (2008).

27. Hadler, M. D., Tzilivaki, A., Schmitz, D., Alle, H. & Geiger, J. R. P. Gamma oscillation plasticity is mediated via parvalbumin interneurons. *Sci. Adv.* **10**, (2024).

28. Park, K. *et al.* Optogenetic activation of parvalbumin and somatostatin interneurons selectively restores theta-nested gamma oscillations and oscillation-induced spike timing-dependent long-term potentiation impaired by amyloid β oligomers. *BMC Biol.* **18**, 7 (2020).

29. Turi, G. F. *et al.* Vasoactive Intestinal Polypeptide-Expressing Interneurons in the Hippocampus Support Goal-Oriented Spatial Learning. *Neuron* **101**, 1150-1165.e8 (2019).

30. Kastellakis, G., Cai, D. J., Mednick, S. C., Silva, A. J. & Poirazi, P. Synaptic clustering within dendrites: An emerging theory of memory formation. *Prog. Neurobiol.* **126**, 19–35 (2015).

31. Hu, H., Gan, J. & Jonas, P. Interneurons. Fast-spiking, parvalbumin$^{+}$ GABAergic interneurons: from cellular design to microcircuit function. *Science* **345**, 1255263 (2014).

32. Tort, A. B. L., Komorowski, R., Eichenbaum, H. & Kopell, N. Measuring Phase-Amplitude Coupling Between Neuronal Oscillations of Different Frequencies. *J. Neurophysiol.* **104**, 1195–1210 (2010).

33. Scheffzük, C. *et al.* Selective Coupling between Theta Phase and Neocortical Fast Gamma Oscillations during REM-Sleep in Mice. *PLoS One* **6**, e28489 (2011).

34. Scheffer-Teixeira, R. *et al.* Theta Phase Modulates Multiple Layer-Specific Oscillations in the CA1 Region. *Cereb. Cortex* **22**, 2404–2414 (2012).

35. Belluscio, M. A., Mizuseki, K., Schmidt, R., Kempter, R. & Buzsáki, G. Cross-Frequency Phase–Phase Coupling between Theta and Gamma Oscillations in the Hippocampus. *J. Neurosci.* **32**, 423–435 (2012).

36. Canolty, R. T. *et al.* High Gamma Power Is Phase-Locked to Theta Oscillations in Human Neocortex. *Science (80-. ).* **313**, 1626–1628 (2006).

37. Judák, L. *et al.* Sharp-wave ripple doublets induce complex dendritic spikes in parvalbumin interneurons in vivo. *Nat. Commun.* **13**, 6715 (2022).

38. Kriener, B., Hu, H. & Vervaeke, K. Parvalbumin interneuron dendrites enhance gamma oscillations. *Cell Rep.* **39**, 110948 (2022).

39. Liao, Z. *et al.* Functional architecture of intracellular oscillations in hippocampal dendrites. *bioRxiv* 2024.02.12.579750 (2024).

40. Fernández-Ruiz, A. *et al.* Gamma rhythm communication between entorhinal cortex and dentate gyrus neuronal assemblies. *Science (80-. ).* **372**, (2021).

41. Hines, M. L. & Carnevale, N. T. The NEURON Simulation Environment. *Neural Comput.* **9**, 1179–1209 (1997).

42. Tukker, J. J., Fuentealba, P., Hartwich, K., Somogyi, P. & Klausberger, T. Cell type-specific tuning of hippocampal interneuron firing during gamma oscillations in vivo. *J. Neurosci.* **27**, 8184–8189 (2007).

43. Sun, Q. *et al.* Proximodistal Heterogeneity of Hippocampal CA3 Pyramidal Neuron Intrinsic Properties, Connectivity, and Reactivation during Memory Recall. *Neuron* **95**, 656-672.e3 (2017).

44. Banke, T. G. & McBain, C. J. GABAergic Input onto CA3 Hippocampal Interneurons Remains Shunting throughout Development. *J. Neurosci.* **26**, 11720–11725 (2006).

45. Fukushima, F. *et al.* Ablation of NMDA Receptors Enhances the Excitability of Hippocampal CA3 Neurons. *PLoS One* **4**, e3993 (2009).

46. Kohus, Z. *et al.* Properties and dynamics of inhibitory synaptic communication within the CA3 microcircuits of pyramidal cells and interneurons expressing parvalbumin or cholecystokinin. *J. Physiol.* **594**, 3745–3774 (2016).

47. Wang, H.-X. & Gao, W.-J. Cell type-specific development of NMDA receptors in the interneurons of rat prefrontal cortex. *Neuropsychopharmacology* **34**, 2028–40 (2009).

48. Turi, G. F. *et al.* Vasoactive Intestinal Polypeptide-Expressing Interneurons in the Hippocampus Support Goal-Oriented Spatial Learning. *Neuron* **101**, 1150-1165.e8 (2019).

49. Vladimirov, N., Tu, Y. & Traub, R. D. Synaptic gating at axonal branches, and sharp-wave ripples with replay: a simulation study. *Eur. J. Neurosci.* **38**, 3435–3447 (2013).

50. Tort, A. B. L. *et al.* Dynamic cross-frequency couplings of local field potential oscillations in rat striatum and hippocampus during performance of a T-maze task. *Proc. Natl. Acad. Sci.* **105**, 20517–20522 (2008).

51. Goldberg, J. H., Yuste, R. & Tamas, G. Ca2+ imaging of mouse neocortical interneurone dendrites: contribution of Ca2+-permeable AMPA and NMDA receptors to subthreshold Ca2+dynamics. *J. Physiol.* **551**, 67–78 (2003).

52. Goldberg, J. H. & Yuste, R. Space matters: Local and global dendritic Ca2+ compartmentalization in cortical interneurons. *Trends Neurosci.* **28**, 158–167 (2005).

53. Nörenberg, A., Hu, H., Vida, I., Bartos, M. & Jonas, P. Distinct nonuniform cable properties optimize rapid and efficient activation of fast-spiking GABAergic interneurons. *Proc. Natl. Acad. Sci. U. S. A.* **107**, 894–9 (2010).

54. Bacci, A., Rudolph, U., Huguenard, J. R. & Prince, D. A. Cellular/Molecular Major Differences in Inhibitory Synaptic Transmission onto Two Neocortical Interneuron Subclasses.

55. Kohus, Z. *et al.* Properties and dynamics of inhibitory synaptic communication within the CA3 microcircuits of pyramidal cells and interneurons expressing parvalbumin or cholecystokinin. *J. Physiol.* **594**, 3745–3774 (2016).

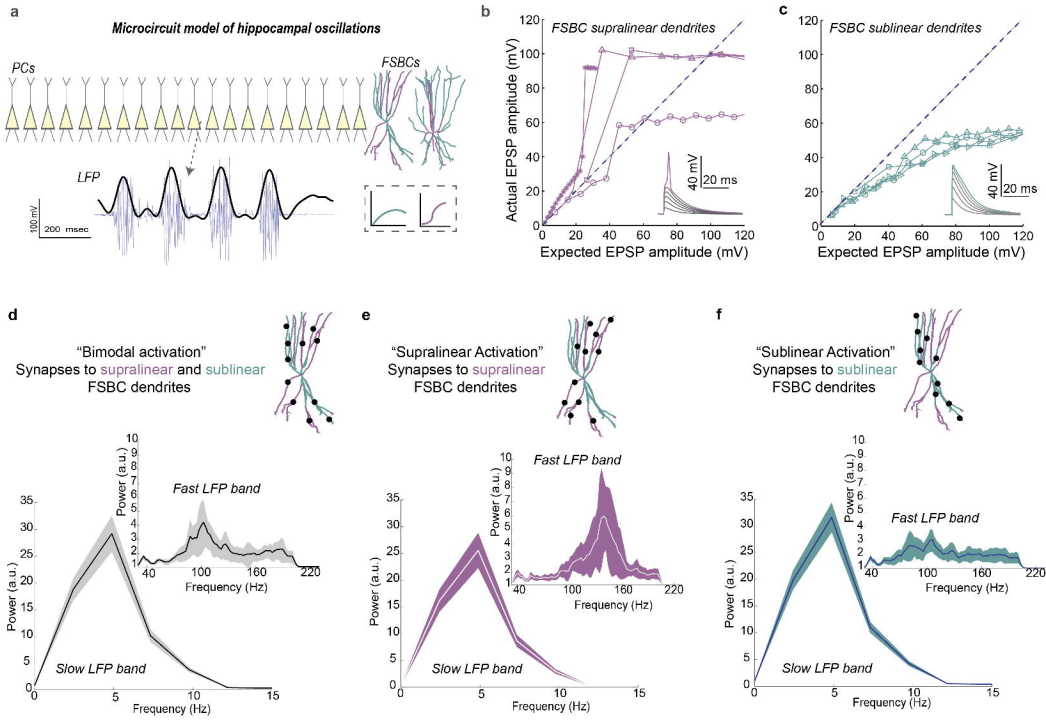
a
Microcircuit model of hippocampal oscillations
PCs
FSBCs
LFP
100 mV
200 msec
b
FSBC supralinear dendrites
Actual EPSP amplitude (mV)
Expected EPSP amplitude (mV)
40 mV
20 ms
c
FSBC sublinear dendrites
Expected EPSP amplitude (mV)
40 mV
20 ms
d
"Bimodal activation"
Synapses to supralinear and sublinear
FSBC dendrites
Fast LFP band
Slow LFP band
Power (a.u.)
Frequency (Hz)
e
"Supralinear Activation"
Synapses to supralinear
FSBC dendrites
Fast LFP band
Slow LFP band
Power (a.u.)
Frequency (Hz)
f
"Sublinear Activation"
Synapses to sublinear
FSBC dendrites
Fast LFP band
Slow LFP band
Power (a.u.)
Frequency (Hz)

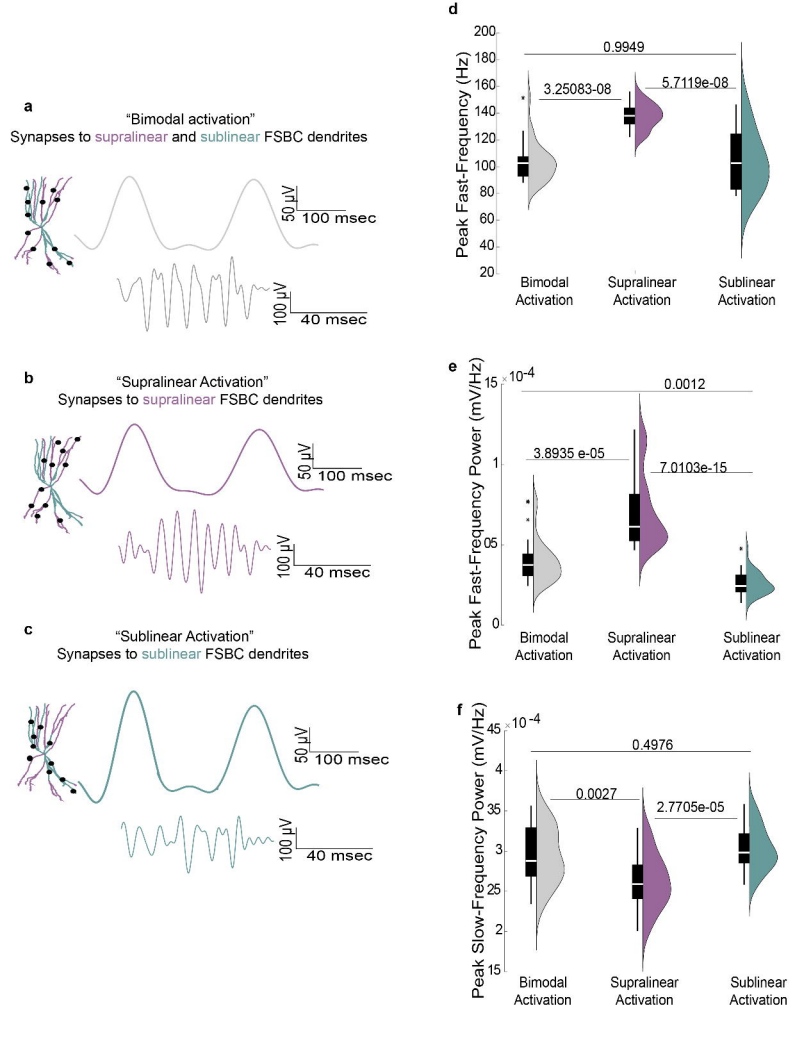
a
"Bimodal activation"
Synapses to supralinear and sublinear FSBC dendrites
50 µV
100 msec
100 µV
40 msec
b
"Supralinear Activation"
Synapses to supralinear FSBC dendrites
50 µV
100 msec
100 µV
40 msec
c
"Sublinear Activation"
Synapses to sublinear FSBC dendrites
50 µV
100 msec
100 µV
40 msec
d
Peak Fast-Frequency (Hz)
0.9949
3.25083-08
5.7119e-08
Bimodal Activation
Supralinear Activation
Sublinear Activation
e
Peak Fast-Frequency Power (mV/Hz)
10-4
0.0012
3.8935 e-05
7.0103e-15
Bimodal Activation
Supralinear Activation
Sublinear Activation
f
Peak Slow-Frequency Power (mV/Hz)
10-4
0.4976
0.0027
2.7705e-05
Bimodal Activation
Supralinear Activation
Sublinear Activation

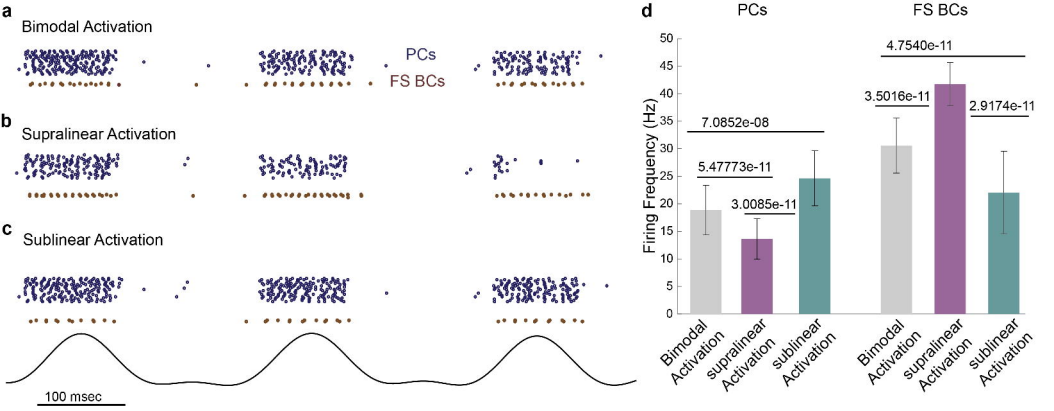
a
Bimodal Activation
PCs
FS BCs
b
Supralinear Activation
c
Sublinear Activation
100 msec
d
PCs
FS BCs
Firing Frequency (Hz)
50
45
40
35
30
25
20
15
10
5
0
7.0852e-08
5.47773e-11
3.0085e-11
4.7540e-11
3.5016e-11
2.9174e-11
Bimodal Activation
supralinear Activation
sublinear Activation
Bimodal Activation
supralinear Activation
sublinear Activation

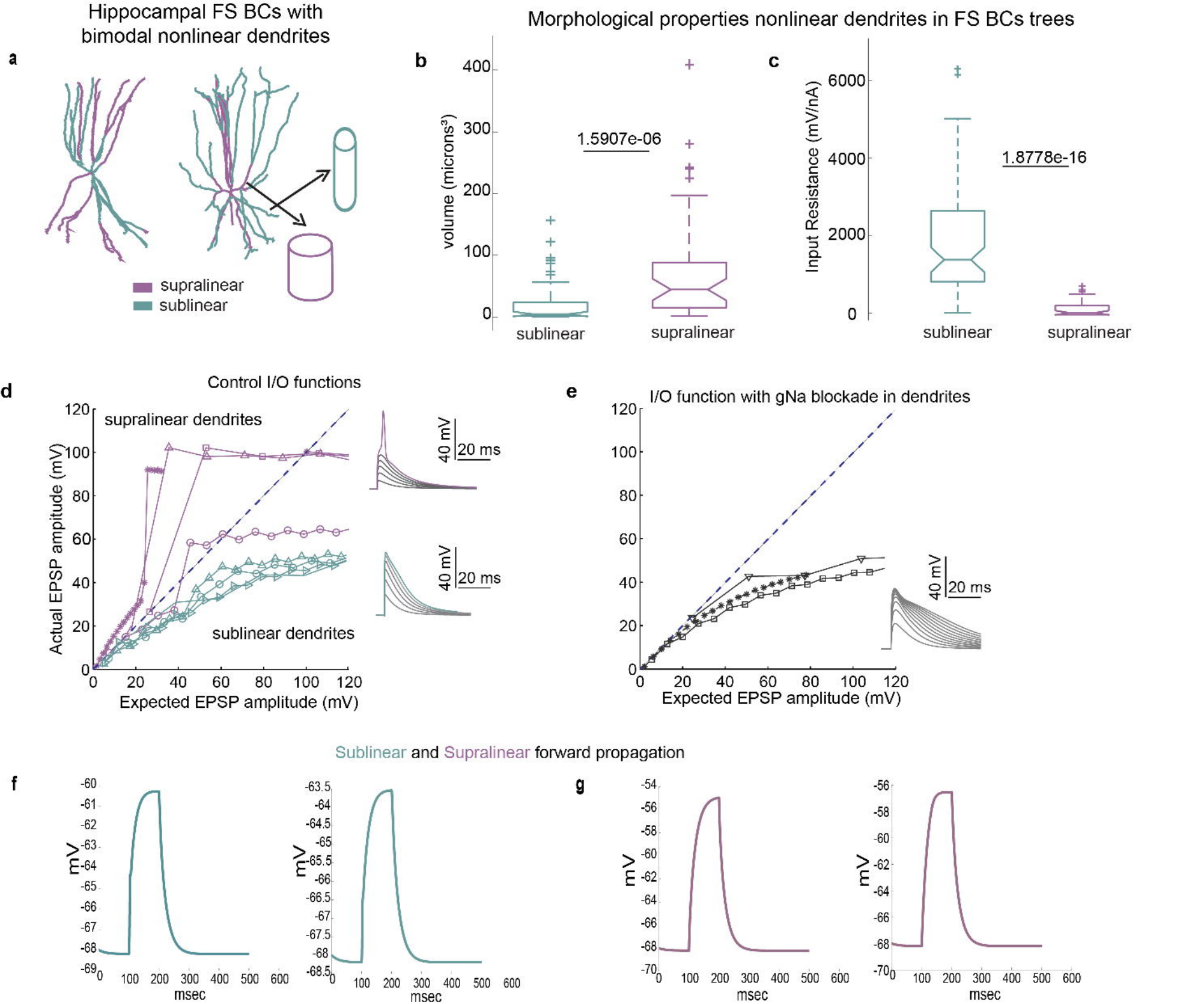
Hippocampal FS BCs with bimodal nonlinear dendrites
a
supralinear
sublinear
Morphological properties nonlinear dendrites in FS BCs trees
b
volume (microns³)
1.5907e-06
sublinear
supralinear
c
Input Resistance (mV/nA)
1.8778e-16
sublinear
supralinear
d
Control I/O functions
supralinear dendrites
sublinear dendrites
Actual EPSP amplitude (mV)
Expected EPSP amplitude (mV)
40 mV
20 ms
e
I/O function with gNa blockade in dendrites
Expected EPSP amplitude (mV)
40 mV
20 ms
Sublinear and Supralinear forward propagation
f
mV
msec
g
mV
msec

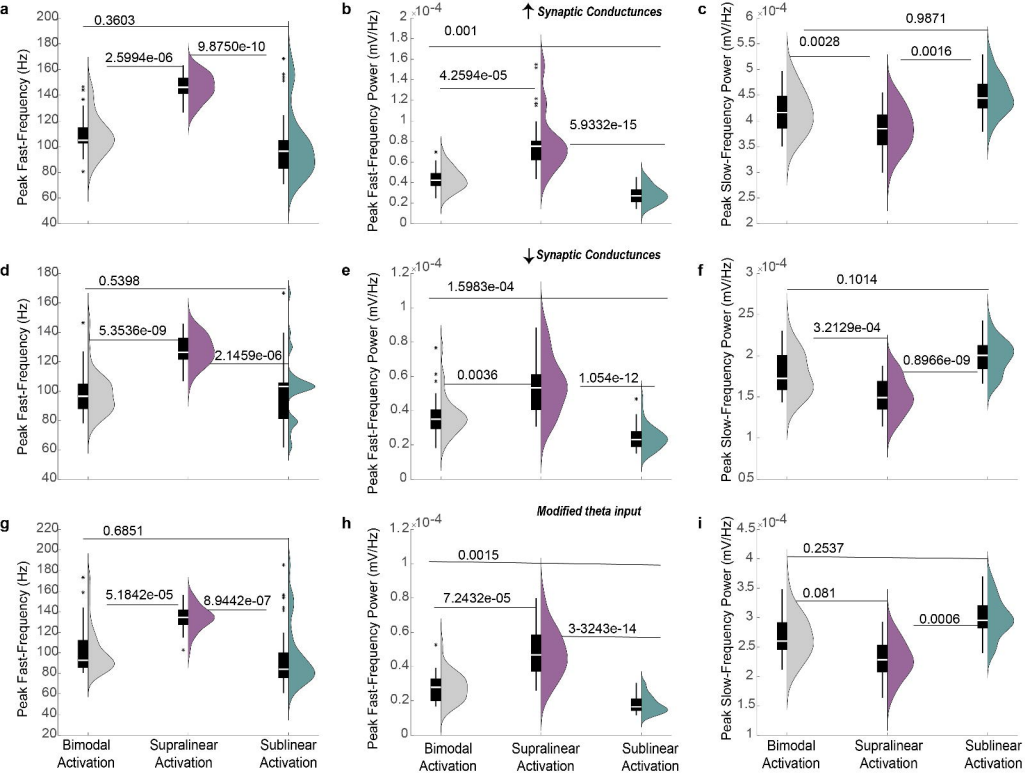
a
Peak Fast-Frequency (Hz)
0.3603
2.5994e-06
9.8750e-10
b
Synaptic Conductunces
Peak Fast-Frequency Power (mV/Hz)
0.001
4.2594e-05
5.9332e-15
c
Peak Slow-Frequency Power (mV/Hz)
0.9871
0.0028
0.0016
d
Peak Fast-Frequency (Hz)
0.5398
5.3536e-09
2.1459e-06
e
Synaptic Conductunces
Peak Fast-Frequency Power (mV/Hz)
1.5983e-04
0.0036
1.054e-12
f
Peak Slow-Frequency Power (mV/Hz)
0.1014
3.2129e-04
0.8966e-09
g
Peak Fast-Frequency (Hz)
0.6851
5.1842e-05
8.9442e-07
h
Modified theta input
Peak Fast-Frequency Power (mV/Hz)
0.0015
7.2432e-05
3-3243e-14
i
Peak Slow-Frequency Power (mV/Hz)
0.2537
0.081
0.0006
Bimodal Activation
Supralinear Activation
Sublinear Activation

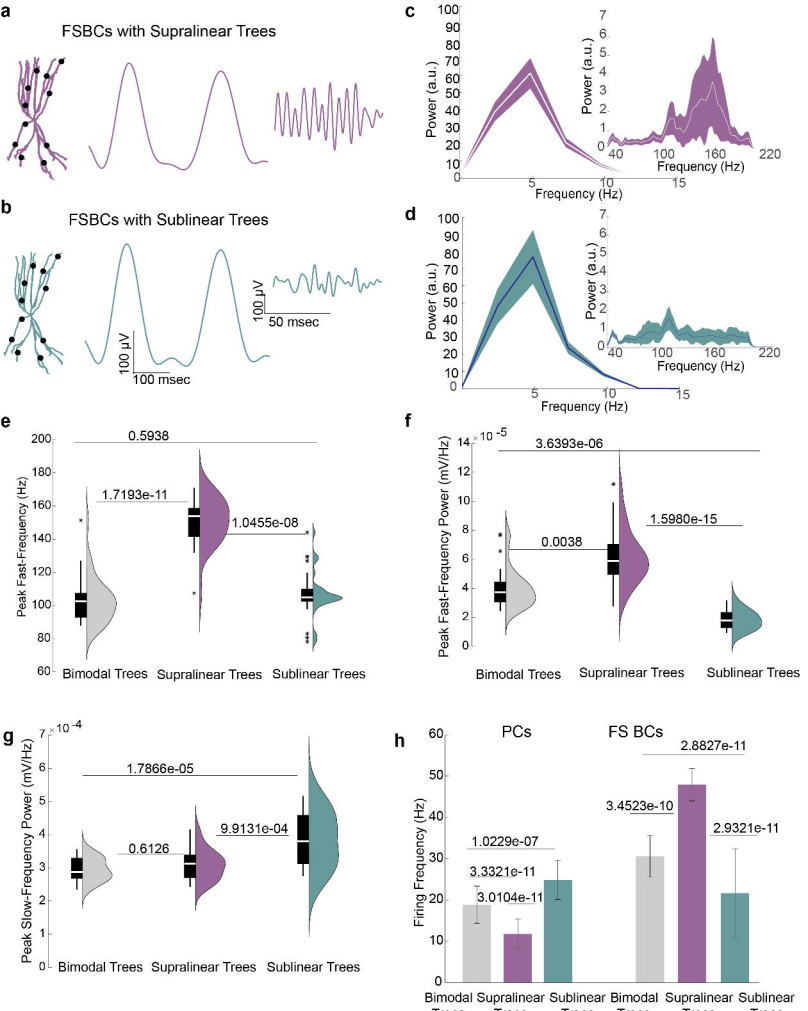
a
FSBCs with Supralinear Trees
b
FSBCs with Sublinear Trees
100 µV
50 msec
100 µV
100 msec
c
Power (a.u.)
Frequency (Hz)
d
Power (a.u.)
Frequency (Hz)
e
Peak Fast-Frequency (Hz)
0.5938
1.7193e-11
1.0455e-08
Bimodal Trees
Supralinear Trees
Sublinear Trees
f
Peak Fast-Frequency Power (mV/Hz)
3.6393e-06
0.0038
1.5980e-15
Bimodal Trees
Supralinear Trees
Sublinear Trees
g
Peak Slow-Frequency Power (mV/Hz)
1.7866e-05
0.6126
9.9131e-04
Bimodal Trees
Supralinear Trees
Sublinear Trees
h
PCs
FS BCs
Firing Frequency (Hz)
1.0229e-07
3.3321e-11
3.0104e-11
3.4523e-10
2.8827e-11
2.9321e-11
Bimodal Trees
Supralinear Trees
Sublinear Trees
Bimodal Trees
Supralinear Trees
Sublinear Trees

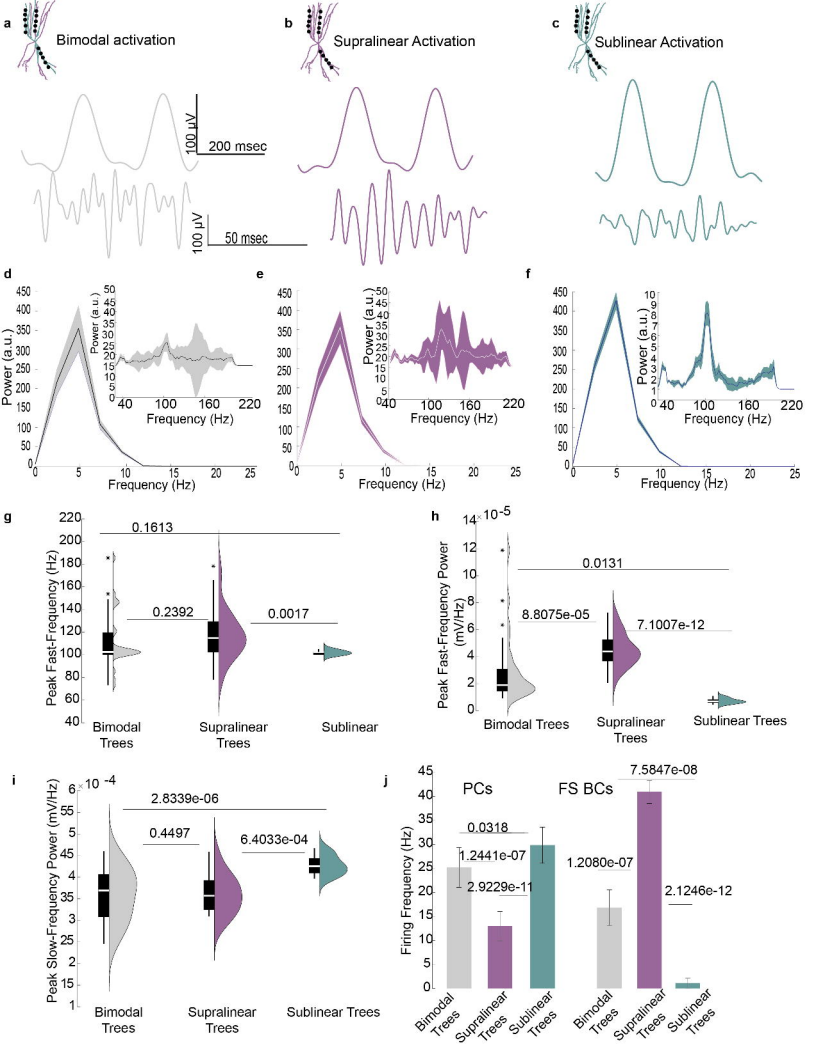
a
Bimodal activation
100 µV
200 msec
100 µV
50 msec
b
Supralinear Activation
c
Sublinear Activation
d
Power (a.u.)
Frequency (Hz)
Power (a.u.)
Frequency (Hz)
e
Power (a.u.)
Frequency (Hz)
Power (a.u.)
Frequency (Hz)
f
Power (a.u.)
Frequency (Hz)
Power (a.u.)
Frequency (Hz)
g
Peak Fast-Frequency (Hz)
0.1613
0.2392
0.0017
Bimodal Trees
Supralinear Trees
Sublinear
h
Peak Fast-Frequency Power (mV/Hz)
10-5
0.0131
8.8075e-05
7.1007e-12
Bimodal Trees
Supralinear Trees
Sublinear Trees
i
Peak Slow-Frequency Power (mV/Hz)
10-4
2.8339e-06
0.4497
6.4033e-04
Bimodal Trees
Supralinear Trees
Sublinear Trees
j
PCs
FS BCs
Firing Frequency (Hz)
0.0318
1.2441e-07
2.9229e-11
7.5847e-08
1.2080e-07
2.1246e-12
Bimodal Trees
Supralinear Trees
Sublinear Trees
Bimodal Trees
Supralinear Trees
Sublinear Trees

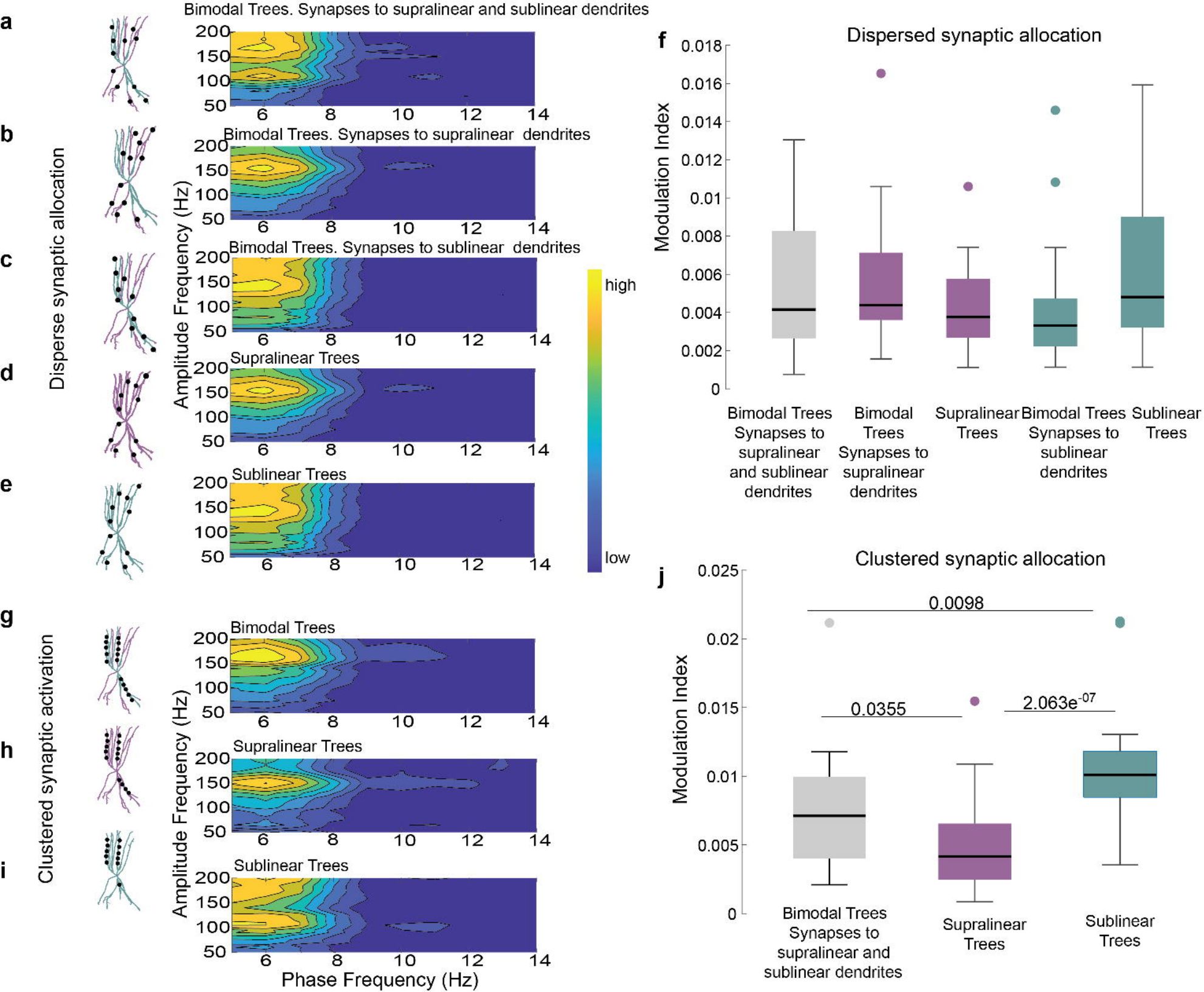
a
b
c
d
e
f
g
h
i
j
Disperse synaptic allocation
Clustered synaptic activation
Bimodal Trees. Synapses to supralinear and sublinear dendrites
Bimodal Trees. Synapses to supralinear dendrites
Bimodal Trees. Synapses to sublinear dendrites
Supralinear Trees
Sublinear Trees
Bimodal Trees
Amplitude Frequency (Hz)
Phase Frequency (Hz)
high
low
Dispersed synaptic allocation
Modulation Index
Bimodal Trees Synapses to supralinear and sublinear dendrites
Bimodal Trees Synapses to supralinear dendrites
Supralinear Trees
Bimodal Trees Synapses to sublinear dendrites
Sublinear Trees
Clustered synaptic allocation
0.0098
0.0355
2.063e-07